IVYSPRING INTERNATIONAL PUBLISHER

Theranostics

2019; 9(8): 2129-2142. doi: 10.7150/thno.31179

Research Paper

Preclinical efficacy of hK2 targeted [^{177}Lu]hu11B6 for prostate cancer theranostics

Oskar Vilhelmsson Timmermand[1]✉, Jörgen Elgqvist[2], Kai A. Beattie[3], Anders Örbom[1], Erik Larsson[4], Sophie E. Eriksson[1], Daniel L.J. Thorek[5], Bradley J. Beattie[6], Thuy A. Tran[7,8], David Ulmert[1,3,9*], Sven-Erik Strand[1,4*]

1. Division of Oncology and Pathology, Department of Clinical Sciences Lund, Lund University, Lund, Sweden
2. Department of Medical Physics and Biomedical Engineering, Sahlgrenska University Hospital, Gothenburg, Sweden
3. Molecular Pharmacology Program, Sloan Kettering Institute, Memorial Sloan Kettering Cancer Center, New York, NY 10065, USA
4. Division of Medical Radiation Physics, Department of Clinical Sciences Lund, Lund University, Lund, Sweden
5. Department of Radiology, Washington University School of Medicine, Saint Louis, MO, 63108, USA.
6. Department of Medical Physics, Memorial Sloan Kettering Cancer Center, New York, NY 10065, USA.
7. Department of Radiopharmacy, Karolinska University Hospital, Stockholm, Sweden
8. Department of Clinical Neuroscience, Karolinska Institutet, Stockholm, Sweden
9. Department of Molecular and Medical Pharmacology, David Geffen School of Medicine at University of California, Los Angeles (UCLA), CA, USA

*Equal contribution

✉ Corresponding author: Division of Oncology, Department of Clinical Sciences Lund, Lund University, Barngatan 4, bottom floor, 221 85 Lund, Sweden. E-mail: oskar.vilhelmsson_timmermand@med.lu.se

Received: 2018.11.02; Accepted: 2019.01.17; Published: 2019.04.06

Abstract

Androgen ablating drugs increase life expectancy in men with metastatic prostate cancer, but resistance inevitably develops. In a majority of these recurrent tumors, the androgen axis is reactivated in the form of increased androgen receptor (AR) expression. Targeting proteins that are expressed as a down-stream effect of AR activity is a promising rationale for management of this disease. The humanized IgG1 antibody hu11B6 internalizes into prostate and prostate cancer (PCa) cells by binding to the catalytic cleft of human kallikrein 2 (hK2), a prostate specific enzyme governed by the AR-pathway. In a previous study, hu11B6 conjugated with Actinium-225 (^{225}Ac), a high linear energy transfer (LET) radionuclide, was shown to generate an AR-upregulation driven feed-forward mechanism that is believed to enhance therapeutic efficacy. We assessed the efficacy of hu11B6 labeled with a low LET beta-emitter, Lutetium-177 (^{177}Lu) and investigated whether similar tumor killing and AR-enhancement is produced. Moreover, single-photon emission computed tomography (SPECT) imaging of ^{177}Lu is quantitatively accurate and can be used to perform treatment planning. [^{177}Lu]hu11B6 therefore has significant potential as a theranostic agent.

Materials and Methods: Subcutaneous PCa xenografts (LNCaP s.c.) were grown in male mice. Biokinetics at 4-336 h post injection and uptake as a function of the amount of hu11B6 injected at 72 h were studied. Over a 30 to 120-day treatment period the therapeutic efficacy of different activities of [^{177}Lu]hu11B6 were assessed by volumetric tumor measurements, blood cell counts, molecular analysis of the tumor as well as SPECT/CT imaging. Organ specific mean absorbed doses were calculated, using a MIRD-scheme, based on biokinetic data and rodent specific S-factors from a modified MOBY phantom. Tumor tissues of treated xenografts were immunohistochemically (IHC) stained for Ki-67 (proliferation) and AR, SA-β-gal activity (senescence) and analyzed by digital autoradiography (DAR).

Results: Organ-to-blood and tumor-to-blood ratios were independent of hu11B6 specific activity except for the highest amount of antibody (150 µg). Tumor accumulation of [^{177}Lu]hu11B6 peaked at 168 h with a specific uptake of 29 ± 9.1 percent injected activity per gram (%IA/g) and low accumulation in normal organs except in the submandibular gland (15 ± 4.5 %IA/g), attributed to a cross-reaction with mice kallikreins in this organ, was seen. However, SPECT imaging with therapeutic amounts of [^{177}Lu]hu11B6 revealed no peak in tumor accumulation at 7 d, probably due to cellular retention of ^{177}Lu and decreasing tumor volumes. For [^{177}Lu]hu11B6 treated mice, tumor decrements of up to 4/5 of the initial tumor

volume and reversible myelotoxicity with a nadir at 12 d were observed after a single injection. Tumor volume reduction correlated with injected activity and the absorbed dose. IHC revealed retained expression of AR throughout treatment and that Ki-67 staining reached a nadir at 9-14 d which coincided with high SA- β-gal activity (14 d). Quantification of nuclei staining showed that Ki-67 expression correlated negatively with activity uptake. AR expression levels in cells surviving therapy compared to previous timepoints and to controls at 30 d were significantly increased ($p = 0.017$).

Conclusions: This study shows that hu11B6 labeled with the low LET beta-emitting radionuclide ^{177}Lu can deliver therapeutic absorbed doses to prostate cancer xenografts with transient hematological side-effects. The tumor response correlated with the absorbed dose both on a macro and a small scale dosimetric level. Analysis of AR staining showed that AR protein levels increased late in the study suggesting a therapeutic mechanism, a feed forward mechanism coupled to AR driven response to DNA damage or clonal lineage selection, similar to that reported in high LET alpha-particle therapy using ^{225}Ac labeled hu11B6, however emerging at a later timepoint.

Introduction

Castration resistant prostate cancer (CRPC) is associated with poor prognosis and is often characterized by sustained AR-signaling over the entire course of disease progression. In fact, 'castrate-resistant' reflects continued androgen dependence, rather than independence [1]. Thus, much of the effort spent developing new pharmacological compounds has been focused on either AR blockade or androgen synthesis deprivation with drugs such as apalutamide and abiraterone. However, despite interventions with these drugs (and often following an initial response), some form of reactivation of the AR pathway inevitably occurs. The radiotherapeutic we consider here follows an alternate line of reasoning. Rather than attempting to disrupt the AR-signaling, we take advantage of its presence by targeting potent cytotoxic agents to proteins resultant from AR pathway activation [2].

The use of radioimmunotherapy (RIT) has been shown to be a successful treatment of liquid tumors using anti-CD20 and CD33 antibodies [2,3]. Radionuclide therapy of CRPC patients using prostate specific membrane antigen (PSMA) targeting modalities are promising but might have severe dose-limitations due to high expression and uptake in off-target organs such as salivary glands and kidneys [4-7].

Human kallikrein related peptidase 2 (hK2) is a serine protease that is exclusively found in prostate tissues (both healthy and malignantly derived) and is known to have increased expression with the severity of the disease [8-11]. *KLK2*, the gene encoding hK2, is regulated by the AR pathway. In a manner similar to that of the closely related kallikrein, Prostate specific antigen (PSA), active hK2 is retrograde released into the blood where it is immediately deactivated by abundant protease inhibitors [12]. We have devised a humanized targeting platform based on the construction of an antibody, hu11B6, which is specific for the catalytic cleft of active hK2. To date, we have shown that hu11B6 specifically internalizes into hK2 expressing cells in vivo through a mechanism that relies on the intact variable region, and on the fragment crystallizable (Fc) region's ability to bind to the neonatal Fc receptor (FcRn) [13].

In a previous study, following therapy with hu11B6 labeled with the high LET alpha-particle emitting radionuclide Actinium-225 (^{225}Ac), we reported an increase in AR-activity and hK2 production in cells as an effect of DNA repair [14]. The AR flair phenomenon has initially been reported based on Caesium-137 (^{137}Cs) external beam radiation [15, 16], and to our knowledge it has not been previously demonstrated that low LET beta-emissions generate the same effect. High LET alpha-particles produce irreparable damage, i.e. DNA double strand breaks (DSB), when traversing the nucleus compared to low LET beta-particles which to a higher degree indirectly damage the cell via the creation of reactive oxygen species [17,18]. This oxidative stress results in DNA single strand breaks (SSB) and a lower frequency of DSB. However, the occurrence of an AR flair phenomenon caused by low LET beta-particles could potentially result in enhanced treatment efficacies relating to a feed-forward mechanism. This is of particular interest since various low LET β-emitters are frequently used in radiotherapeutic agents.

The overarching aim of the current study was to gather dosimetric, therapeutic and radiobiological data that will guide our upcoming clinical translation of radiolabeled hu11B6. In this study we investigated whole body and small-scale tumor dosimetry in an animal model, as well as therapeutic and biological effects of hu11B6 labeled with Lutetium-177 (^{177}Lu), a low LET beta-emitter with significant interest for theranostic clinical RIT.

Materials and methods

Conjugation, radiolabeling and affinity measurements of hu11B6

Conjugation, radiolabeling and stability studies were performed as previously described [18]. In summary, hu11B6 and non-specific isotype control IgG_1 were conjugated with p-SCN-Bn-CHX-A"-DTPA (Macrocyclics, Dallas, TX), a backbone substituted diethylenetriaminepentaacetic acid (DTPA) derivate chosen as a trade-off between stability and metal ion complexation [19], in a 1:3 molar ratio. 50 – 250 MBq $^{177}LuCl_3$ (IDB Petten BV, Baarle-Nassau, Holland) was added to 150 µg of hu11B6 (~1 µg/µL) in ammonium acetate buffer (pH of ~5.5), with a final volume of 500 µL. After 2 h of incubation, free ^{177}Lu was eluted from ^{177}Lu-DTPA-hu11B6 ([^{177}Lu]hu11B6) and ^{177}Lu-DTPA-IgG_1 ([^{177}Lu]IgG_1) using a NAP-5 column (GE Healthcare, Uppsala, Sweden) equilibrated with saline or PBS. Stability of [^{177}Lu]hu11B6 was studied by incubating samples (n = 3) in mouse serum at 37°C for 1 w, using labeled conjugate in PBS as a control. Separation was performed on NuPAGE®Bis-Tris Gel (Life technologies via Thermo Fischer Scientific). The conjugation and radiolabeling of the non-specific antibody, an IgG antibody from mouse serum (Sigma, I-8765), was performed as above. Binding affinity of ^{177}Lu-hu11B6 was evaluated and compared to non-labeled hu11B6 using Surface Plasmon Resonance (SPR), see suppl. information.

Cell line

LNCaP-FGC was purchased from American Type Culture Collection (ATCC, Manassas, VA) and cultured according to their instructions.

Animal model

All animal experiments were performed in accordance with the regional Ethics Committee's requirements. Male BALB/c foxn1^{nu}/foxn1^{nu} (in house) or NMRI foxn1^{nu}/foxn1^{nu} (Charles River Laboratories, Wilmington, MA) were inoculated subcutaneously in the right flank with the *KLK2* expressing cell line LNCaP-FGC in a suspension of 1:1 mixture of RPMI-1640 media and Matrigel (BD Biosciences, San Jose, CA). Due to the technical difficulties of sampling enough blood related to the size of BALB/c foxn1^{nu}/foxn1^{nu} mice, the relatively larger NMRI nude mice were added to obtain a complete picture of the blood status but not included in the survival analysis.

Specific activity and biodistribution study

Mice bearing LNCaP s.c. xenografts (n = 3 - 4 per group) were administered fixed activities of [^{177}Lu]hu11B6 by tail-vein injections (0.4 - 0.6 MBq). The mass amounts of hu11B6 injected were however varied; 10, 30, 50, 100, 150 µg. Tumors, blood, and organs were collected at 72 h post-injection. A separate set of mice bearing LNCaP s.c. xenografts was administered with a roughly fixed specific activity of [^{177}Lu]hu11B6 (20 - 30 µg of protein and 0.4 - 0.6 MBq of ^{177}Lu) but in this case tumors, blood, and organs were collected at 4, 24, 48, 72, 168 and 336 h post-injection. Animals were euthanized using intra-peritoneal injections of Ketalar-Rompun (10 µL/g, bodyweight), or via carbon dioxide inhalation, followed by heart puncture and collection of blood. Harvested tissues were weighed and measured in a NaI(Tl) well counter (1480 Wizard, Wallac, Perkin Elmer) and compared to radioactive standards. The count data were background and decay corrected, and uptake was expressed as percent injected activity per gram of tissue (%IA/g).

SPECT/CT

A preclinical SPECT/CT scanner (NanoSPECT/CT Plus, Mediso; Budapest, Hungary) equipped with the NSP-106 multipinhole mouse collimator was used and with energy windows of 20% centered over the 56-, 113-, and 208-keV energy peaks of ^{177}Lu. Acquisition time was about 40 min. Mice given therapeutic amounts of [^{177}Lu]hu11B6 and dedicated for molecular tumor analysis (see section on therapeutic efficacy) were imaged at 4, 7, 9 and 14 d (n = 4) post injection. CT imaging was done before each whole-body SPECT. SPECT data was reconstructed using HiSPECT software (SciVis; Goettingen, Germany). With the help of the CT images as an anatomical reference, regions of interest (ROI), where drawn for tumor, submandibular glands, liver and heart using the VivoQuant 3.0 software (inviCRO; Boston, MA). Activity data (MBq/mm^3) was extracted and then converted to percent injected activity per gram of tissue (%IA/g) by assuming a tissue density of 1.0 g/cm^3.

Therapeutic efficacy

LNCaP tumor bearing mice (tumor > 3mm in diameter) were randomized to one of seven groups, with one group randomized for molecular tumor analysis using pre-set euthanization time-points at 4, 9, 14 and 30 d after initiation of treatment and with one group left untreated. All mice were administered a single injection having a protein mass of 30 µg, determined based on previous results [20] and on the results of the aforementioned specific activity study. Syringe activity (MBq) was measured before and after injection (Atom Lab 500 Dose Calibrator, Biodex Medical Systems Inc., Shirley, NY) to determine the

range of individually injected activity (Table 1). Bodyweight and tumor volume (external caliper measurement, V = 0.5 × length × width × width) were monitored 2–3 times per week up to 120 d post injection. For tumor size range at start of therapy, see the Supplementary Information section. Relative tumor size (RTS) was calculated as the natural logarithm of the fractional increase in volume relative to the tumor size at treatment start [21]. Tumor diameter >15 mm, or severe decline in general condition, were used as endpoints. The total white blood cell counts (WBC), red blood cell counts (RBC) and platelets (PLT) were measured twice weekly during the first month. Blood samples (20 µL) were collected from the tail vein and analyzed in an Exigo Veterinary (Exigo Vet) Hematology Analyzer (Boule Medical, Stockholm, Sweden).

Immunohistochemistry and androgen receptor intensity analysis

After mice were euthanized, tumor tissue was collected, portioned and cryo-preserved in optimal cut temperature cryomount (Histolab Products AB, Stockholm, Sweden), or first fixed in 4% paraformaldehyde (PFA) solution and embedded in paraffin before sectioning. Prior to staining for Ki-67 and AR, cryosections were dried for 15 min in 37°C and then fixed with 4% PFA and quenched for 5-10 min using Dako REAL Peroxidase blocking solution (Agilent Technologies, Santa Clara, Ca, US), then incubated with rabbit anti-Ki-67 mAb (Clone SP6, Thermo Fischer Scientific) or anti-AR mAb (ab133273, Abcam, Cambridge, UK) respectively, followed by a 1 h incubation with horseradish peroxidase conjugated Goat anti-rabbit $F(ab)_2$ (111-036-045, Jackson ImmunoResearch Laboratories, Inc., West Grove, PA) and developed with Dako liquid DAB+ substrate-chromogen system (Agilent Technologies). For detection of SA-β-gal activity, a marker of senescence, the Abcam senescence detection kit (ab65351) was used on cryosections first dried for 15 min in 37°C and then fixed in 1% formalin for 1 min (fixative solution from kit). After counterstaining with hematoxylin, or in the case of SA-β-gal activity, with nuclear fast red solution (Sigma-Aldrich, Saint Louis, Mo) and mounting with Pertex (Histolab), the sections were imaged using a MIRAX MIDI automated whole slide imager (Carl Zeiss AG, Oberkochen, Germany). The Ki-67, AR and SA-β-gal stained sections were independently evaluated by two skilled observers and graded from no visible staining (-) to the most intense staining (+++).

Sections from paraffin embedded blocks were also used together with a modified AR staining protocol where the concentration of anti-AR mAb was eight times lower than previously. This resulted in tissue section images with a range of AR expression intensities (as opposed to the effectively binary staining achieved when high concentration of anti-AR mAb was applied). These sections were analyzed as follows. Masks selecting the AR expressing cells within the images were generated using the Color Threshold, Make Binary and Analyze Particle functions within ImageJ [22]. These masks were then applied to the original images (in RGB format) and inverted mean-cell-intensities were calculated using code written in Matlab (MATLAB and Statistics Toolbox Release 2012b, The MathWorks, Inc., Natick, Massachusetts, United States).

Macro- and small-scale dosimetry

Mean absorbed dose was calculated using a previously described MIRD-scheme with mouse-specific S-factors [20, 23]. For calculation of organ/tumor S-factors relevant for the used animal model, a version of the MOBY phantom [24] was applied. Actual organ sizes were used as input for the S-value calculations using the Monte Carlo package MCNP6. Bi-exponential curves were fitted to the biokinetic data by least-square-fit to calculate the time-integrated activity coefficient (see suppl. information). The absorbed dose to the bone marrow was calculated based on the assumption that the activity concentration in red marrow is proportional to blood at a ratio of 0.36 [25].

DAR of xenograft cryosections was performed using a Biomolex 700 Imager (Biomolex AS, Oslo, Norway) having an intrinsic spatial resolution of 50 µm and a ^{177}Lu detection efficiency as previously reported [26]. Corrections were applied for dead or miscalibrated detector strips and radioactive decay. To scale to specific uptake, each pixel was assumed to contain a tissue volume of 50x50x8 μm^3 and have a density of 1.0 g/cm^3. Autoradiographic images were analyzed using IDL 8.5 (Exelis VIS, Harris Corporation) and ImageJ. The absorbed-dose rate distribution was calculated using a dose point kernel (DPK) acquired by Monte Carlo simulation [27]. All layers along one axis of the three-dimensional DPK were summed to form a two-dimensional DPK that includes contributions from assumed identical activity distributions above and below the imaged sections. The image resolution was then down-sampled to 100 µm pixels to match the DPK before convolution was performed to produce absorbed-dose rate images. Correlation between specific uptake or absorbed dose rate and cell proliferation was evaluated by comparing three to six ROIs, each about 1.3 ± 1.1 mm^2, drawn using ImageJ on each image along with an identical ROI in the

adjacent Ki-67 stained slide [28]. The intensity of staining per nuclear area in these images was determined using the ImageJ Immunoratio plugin [29] with the threshold set to the maximum level to avoid false positive classification of hemochromatic areas as an effect of the RIT. Correlation was tested with the non-parametric Spearman correlation measure using IBM SPSS Statistics version 23.

Statistical and Image Analysis

Data are presented as the mean ±SD and statistical significance was analyzed using the *t*-test, unless otherwise noted. In all cases, differences in results were taken to be statistically significant with computed $p < 0.05$. Linear regression was applied to evaluate treatment and dose response. Median survival was calculated from Kaplan Meier graphs generated with Prism 4. Statistical analyses were performed using GraphPad Prism version 4 (GraphPad Software Inc., San Diego, CA), IBM SPSS Statistics version 23 (SPSS Inc., Chicago, IL) and Excel 2016 (Microsoft).

Results

Conjugation, Radiolabeling, Stability and Affinity

The labeling yield for [^{177}Lu]hu11B6 was 85.1 ± 5.2% (n = 7) with a radiochemical purity of >99% (n = 7). The stability of [^{177}Lu]hu11B6 in plasma and PBS was 68± 5% (n = 3) and 70% (n=1) at one week, respectively. The affinity constant for conjugated hu11B6 was not found to be significantly different when compared to non-conjugated hu11B6 (p = 0.18) (see suppl. information).

Specific activity and Biodistribution

Organ-to-blood ratios were largely unaffected by specific activity except for at the highest amount of antibody (150 µg), which resulted in higher uptake in lung, spleen and muscle tissues (Figure 1A). Tumor-to-blood ratios (Figure 1B) seem to be lower at higher amounts of antibody, possibly due to competitive inhibition, however they did not differ significantly between the groups (non-parametric

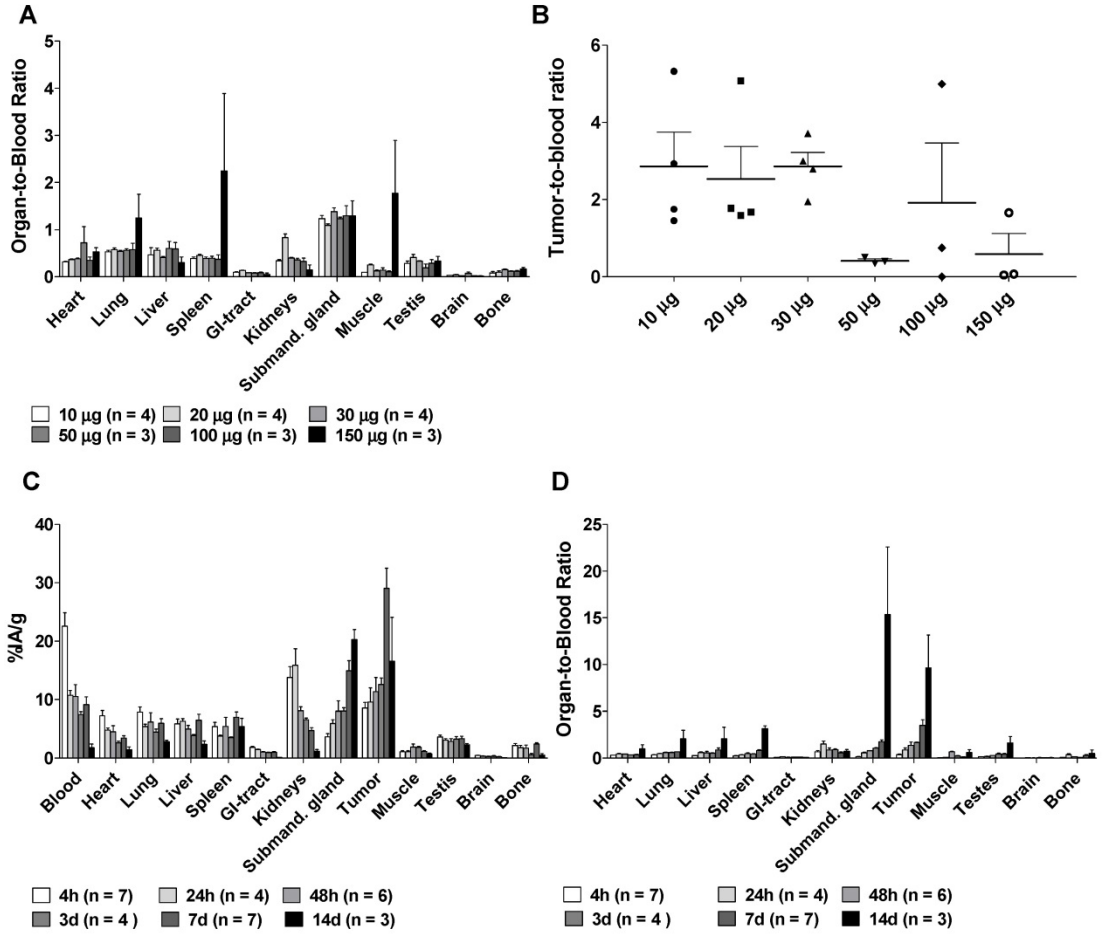

Figure 1. A. The Organ-to-blood ratio for 10-150 µg labeled hu11B6 at 72h, uptake in the studied normal organs do not seem to change with increasing antibody amount up to 150 µg. **B. The Tumor-to-blood ratio** for 10-150 µg labeled hu11B6 at 72h, the tumor to blood ratio varies and seem to be lower at higher amounts of antibody, possibly because of competitive inhibition, however the variation is not statistically significant (p = 0.07). **C. The Biokinetics of 177Lu-hu11B6 (20-30 µg).** Tumor uptake increased up to 1 w p.i. Generally, normal organs had far less accumulation of the tracer compared to tumor, except for the submandibular glands (as a cross-reaction between human hK2 and a species specific kallikrein found in rodent salivary glands). **D. Organ-to-blood ratio** for ^{177}Lu-hu11B6 versus time derived from data in Figure 1C.

Kruskal-Wallis test, p = 0.07). Peak tumor specific uptake (29.1 ± 9.1 %IA/g) was noted at 1 w, and maximum tumor-to-blood ratio 9.6 ± 6.1 was noted at 14 days, with blood clearance as the major reason for this increase (Figure 1C-D), which corresponds well with previously reported results [13, 20]. Uptake of [^{177}Lu]hu11B6 was also noted in the submandibular glands. This finding is unrelated to humans and has previously been reported as a possible cross-reaction between 11B6 and a non-specified species-specific kallikrein expressed in rodent salivary glands [13, 20]. The accumulation in the submandibular glands was 15 ± 5 %IA/g at one week which can be compared with the residual activity in other normal organs at between 0.2 -7.0 %IA/g at the same time (Figure 1C). Compared to other non-kallikrein expressing organs, clearance of [^{177}Lu]hu11B6 was slower in the liver and spleen, organs known to degrade full-sized antibodies (Figure 1D).

SPECT/CT

Representative SPECT/CT images for 4, 7, 9 and 14 days are displayed in Figure 2A. The specific uptake (%IA/g) calculated from the SPECT acquisition followed a different trend in xenografts as compared to the biodistribution with subtherapeutic amounts of activity (compare Figure 1C and Figure 2B). Instead of peaking at 7-9 d the specific uptake continued to increase with time. The difference could be explained by the therapeutic absorbed doses delivered by the amount of [^{177}Lu]hu11B6 used for SPECT imaging. Over time this leads to decrease in tumor volume, e.g. the group of mice imaged at 7 and 14 d, had a tumor size reduction of about 50% within a week. This is further supported by the small change in %IA for the same group (Figure 2C). The normal organs follow a similar trend as compared to the biodistribution, except for the submandibular glands (compare Figure 1C and Figure 2B). This could be due to the difficulty of drawing ROIs over the glands or from effects of treatment reducing the specific uptake.

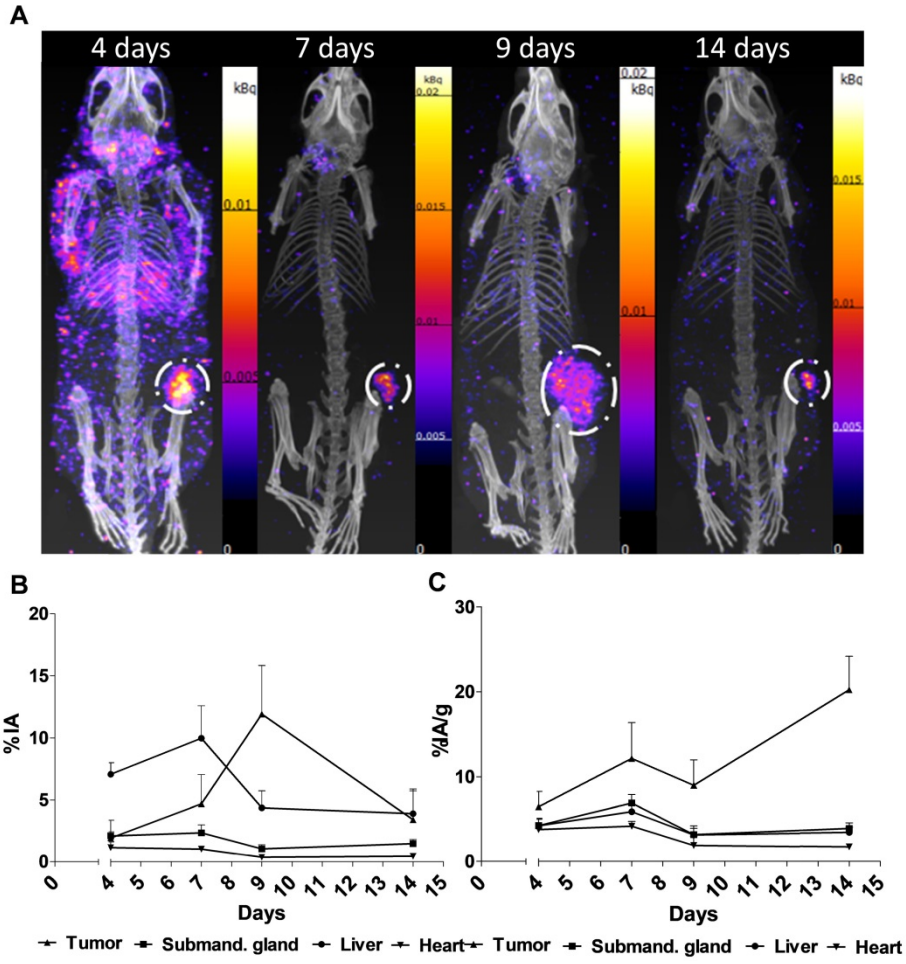

Figure 2. SPECT/CT imaging A. Representative maximum intensity projections of SPECT/CT of mice at 4, 7, 9 and 14 days p.i. of ^{177}Lu-hu11B6. B. Biokinetics as %IA/g of therapeutic amounts of ^{177}Lu-hu11B6 (20-30 µg) quantified from SPECT data. Quantified data from SPECT/CT imaging of ^{177}Lu-hu11B6 for tumor, submandibular gland, liver and heart. The tumor biokinetics for therapeutic amounts of ^{177}Lu-hu11B6 is different from that seen in Figure 1C, the %IA/g continues to increase after 7d, probably as an effect of internalization of ^{177}Lu-hu11B6 and tumor shrinkage following therapy. **C. Quantified %IA data from SPECT/CT imaging of ^{177}Lu-hu11B6.** Evidently, while the group at nine days had a lower %IA/g it has a higher %IA. This is due to a somewhat larger tumor size in this group. It is probable that the high uptake in the xenografts of this group reduces the amount of ^{177}Lu-hu11B6 in other organs.

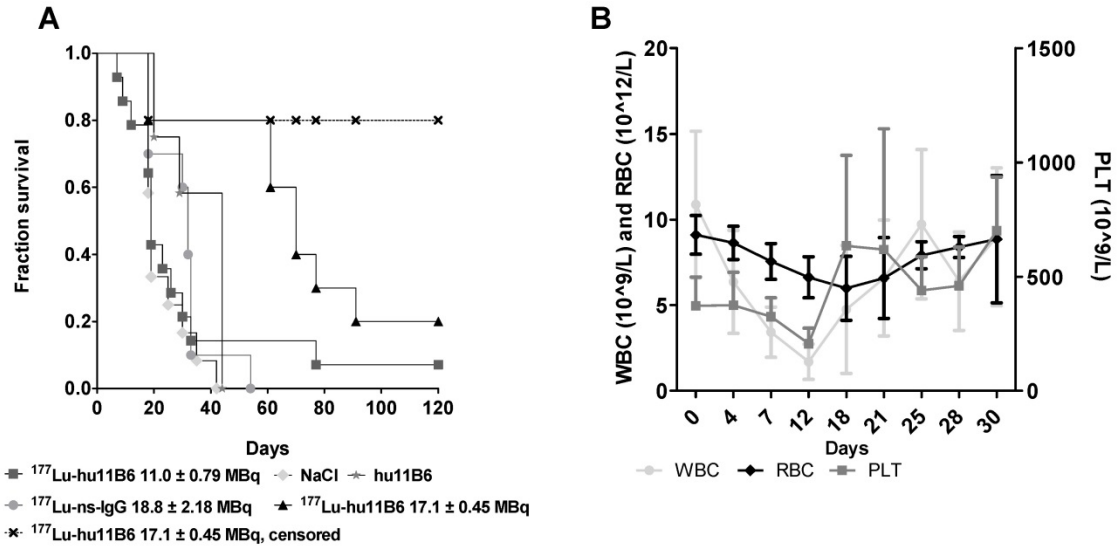

Figure 3. A. Kaplan-Meier survival curve for the therapy and control groups. **Square:** ^{177}Lu-hu11B6, group A, with a median survival of 19 days. Triangle: ^{177}Lu-hu11B6, group B, uncensored (all animals), median survival 77 days; Cross: ^{177}Lu-hu11B6, group B, censored with a median survival beyond 120 days; Stars: unlabeled hu11B6 median survival 44 days; Circle: ^{177}Lu-non-specific mAb median survival 33 days; Diamond: Vehicle median survival 23 days. **B. Hematopoietic toxicity for the therapy group NMRI-foxn1^{nu}/foxn1^{nu}.** From dosimetry the absorbed dose to bone marrow was estimated to 7.2-8.8 Gy showing a nadir at about 12 days for white blood cells and 18 days for red blood cells where after recovery is seen. The absorbed dose to the tumor in this group was estimated to 56-68 Gy.

Therapeutic Efficacy

During the first 30 days of therapy the dominant factor affecting survival was the pre-set tumor size endpoint, not treatment toxicity, and survival is therefore in general well reflected in the log(RTS) of the different groups. Median survival in mice treated with an absorbed dose of 48-53 Gy to the tumor (16.3 - 18.0 MBq of injected activity) was about twice the average median survival of the control groups (Figure 3A). Unfortunately, some subjects had to be euthanized prematurely due to non-tumor size related health issues (tail necrosis resulting from the blood sampling, eye infections and xenograft ulceration). These cases were censored to obtain a tumor growth relevant read-out of the therapeutic effect (Figure 3A). Monitoring of the hematological status in [^{177}Lu]hu11B6 treated mice showed a temporary decline during the first 12 days. At nadir the levels of white blood cells, red blood cells and platelets were 1.7± 1.0 10^9/L, 6.6± 1.2 10^{12}/L and 207± 68 10^9/L, respectively (Figure 3B).

Compared to control groups ([^{177}Lu]IgG$_1$, vehicle and non-labeled hu11B6), [^{177}Lu]hu11B6 treated mice showed a decrease in tumor volumes or significantly reduced growth rates and xenografts given 48-53 Gy to the tumor remained indolent between 25-60 days (Table 1, Figure 4A and suppl. information Figure S2). A single injection of [^{177}Lu]hu11B6, corresponding to tumor absorbed doses of 30-38 Gy (10.2 - 12.7 MBq of injected activity), 48-53 Gy (16.3 - 18.0 MBq of injected activity) and 56-68 Gy (18.9 - 23.1 MBq of injected activity) at 25 days, resulted in RTS of 1.5 ± 0.2 (n = 10), 0.29 ± 0.07 (n = 8) and 0.22 ± 1.17 (n = 9), respectively. In corresponding control groups, RTS in [^{177}Lu]IgG$_1$, vehicle and non-labeled hu11B6 treated groups were 2.4 ± 0.8 (n =8), 2.2 ± 0.4 (n = 10) and 6.6 ± 0.8 (n = 12), respectively, at 23 days. However, mice receiving very high levels of activity (1650 ± 131 MBq/kg of [^{177}Lu]hu11B6) had to be euthanized at day 10−12 p.i. due to poor general condition. The administrated activity to this group corresponds to a bone marrow absorbed dose of 15-16 Gy, which is above the reported maximum tolerable absorbed dose to bone marrow in mice [30]. These results were not found to be significantly different from previously reported data based on ^{177}Lu-labeled non-humanized 11B6 murine IgG$_1$ and are included in Table 1 and Figure 4A for comparison [20].

Dosimetry, DAR based small-scale dosimetry and Immunohistochemistry

The average total tumor mean absorbed dose calculated from biodistribution data was approximately 3 Gy/MBq, which is approximately six times higher than most normal organs. Importantly, the total absorbed dose was only 0.4 Gy/MBq in bone marrow, which is about 10 times lower than the absorbed dose to the tumor (Table 1, S3 suppl. information).

Analysis of DAR images showed that the mean absorbed dose rate increased over the first 14 days of the study period (Figure 5A). The small-scale dosimetry performed on sections of tumors at different time points revealed that there is a heterogeneous absorbed dose rate distribution within the tumor. As can be seen in Figure 5A, the maximum and mean absorbed dose rates differ by as much as a

factor of five. This means that a portion of the tumor receives much higher absorbed doses. The comparisons with the mean absorbed dose rate calculated from the biokinetics clearly show great variability of absorbed dose rate, findings that could not be discovered using a dosimetry based on biodistribution data only. An increasing ratio of maximum over mean absorbed dose rate over time indicated that the activity concentrates into smaller areas over the observed period (Figure 5B), which is to be attributed to internalization and lysosomal degradation of [^{177}Lu]hu11B6 in target cells and a decreasing number of vital cells per tissue area. This conclusion is further supported by the SPECT data (Figure 2B) where retention of [^{177}Lu]hu11B6 as the tumor decreases manifests as an increasing specific uptake (%IA/g). During the earlier time-points, high activity could be noted in stromal tissues representing blood activity.

Table 1. **The experimental design** with amongst others the administered activity (MBq), specific activity (MBq/kg) and tumor and bone marrow dosimetry for the [^{177}Lu]hu11B6 therapy study with seven (A-G) groups of animals. Included are data from our previous study with the murine 11B6 antibody [18]. The range of tumor volumes at therapy start are presented in table S1 in the supplementary data. Administered amount of [^{177}Lu]hu11B6 was 20-30 µg.

Group	*n*	Treatment	Administered Activity (MBq)	Specific Activity (MBq/kg)	Weight at injection (g)	Range of Administered Activity (MBq)	Range of Specific Activity (MBq/kg)	Range of Absorbed Dose to tumor** (Gy)	Range of Absorbed Dose to bone marrow** (Gy)
BALB/c-foxn1^{nu}/foxn1^{nu} ^{177}Lu-hu11B6									
A	14	^{177}Lu-hu11B6	11.0 ± 0.8	512 ± 85	22 ± 3	10.2 – 12.7	425 - 704	30 – 38	3.8 – 4.9
B	10	^{177}Lu-hu11B6	17.1 ± 0.5	674± 59	25 ± 3	16.3 – 18.0	610 - 782	48 – 53	6.2 – 6.9
C	9	^{177}Lu-hu11B6	41.2 ± 1.5	1650 ± 131	25 ± 2	39.5 – 42.3	1413 - 1804	117 – 124	15 – 16
D	8	^{177}Lu-ns- mAb	18.8 ± 2.2	802 ± 140	24 ± 2	13 – 20.5	550 - 950	-	-
E	12	hu11B6	–	-		–	-	-	-
F	13	Vehicle	–	-		–	-	-	-
NMRI-foxn1^{nu}/foxn1^{nu} ^{177}Lu-hu11B6									
G	21	^{177}Lu-hu11B6	20.9 ± 1.3	586 ± 54.3	35.8 ± 2.8	18.9 – 23.1	483 - 670	56 – 68	7.2 – 8.8
NMRI-foxn1^{nu}/foxn1^{nu} ^{177}Lu-m11B6* **									
H	5	^{177}Lu-m11B6	10.1 ± 1.2	330 ± 25	30.6 ± 3.0	7.83 – 11.5	301 - 372	23 – 34	3.0 – 4.0
I	6	^{177}Lu-m11B6	19.1 ± 1.4	649 ± 102	30.8 ± 3.0	17.4 – 21.1	512 - 812	51 – 62	6.6 – 8.0
J	3	^{177}Lu-m11B6	36.2 ± 0.7	1080 ± 68	33.7 ± 2.9	35.2 – 37.0	1000 - 1128	104 – 109	13 – 14

Values are, when applicable, presented as mean ± SD. * As calculated based on the biodistribution study shown in Figure 1C. and the average organ weights of the BALB/c foxn1^{nu}/^{nu} therein. ***Original data published elsewhere, Vilhelmsson Timmermand et al. [18]

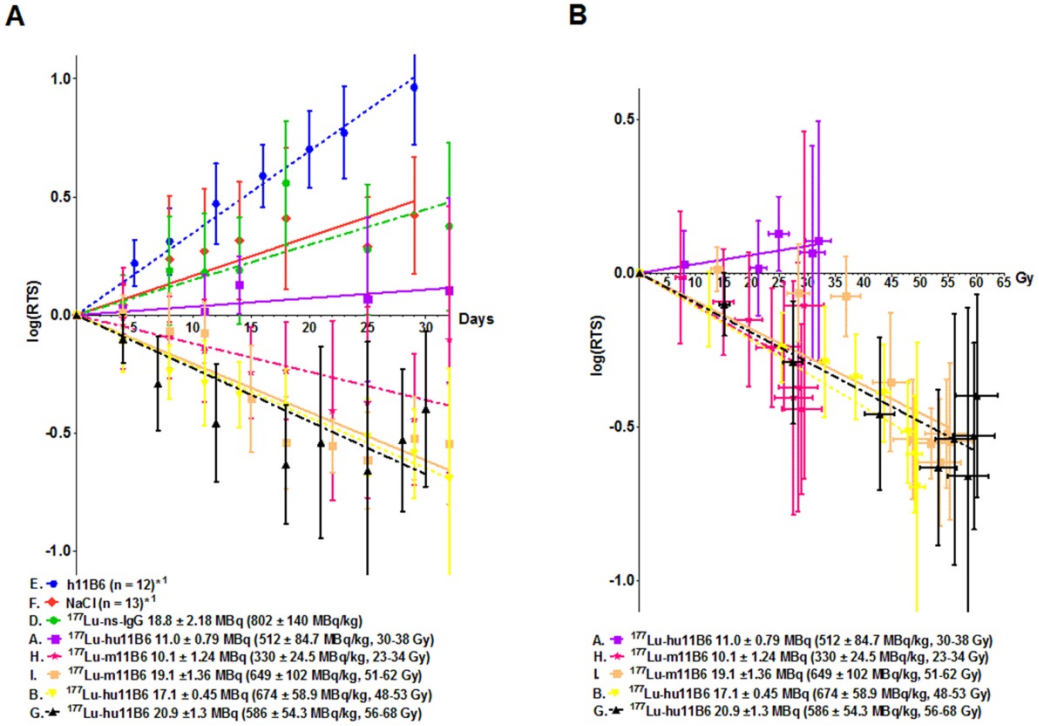

Figure 4. Linear regression of the logarithm of the relative tumor size (log(RTS) +/- SD). This method was applied for the initial 30 days' growth and growth delay data analysis. **A.** The log(RTS) over time for all the therapy groups with ^{177}Lu-hu11B6. Also included the data previously presented [18] for the murine antibody 11B6. Both the humanized and murine 11B6 shows similar therapeutic efficacy. Even though no tumor decrease in group A is observed, there is a growth delay compared to the controls (E, F, D). **B.** The log(RTS) versus tumor absorbed dose, albeit at different dose rates, for all the therapy groups. As can be seen there is almost a linear correlation showing a similar absorbed dose dependent therapeutic efficacy in all groups except in group A. This pattern is recognizable among data from both the humanized, hu11B6 (A, B, G) and the previously published murine (H, I) antibody.

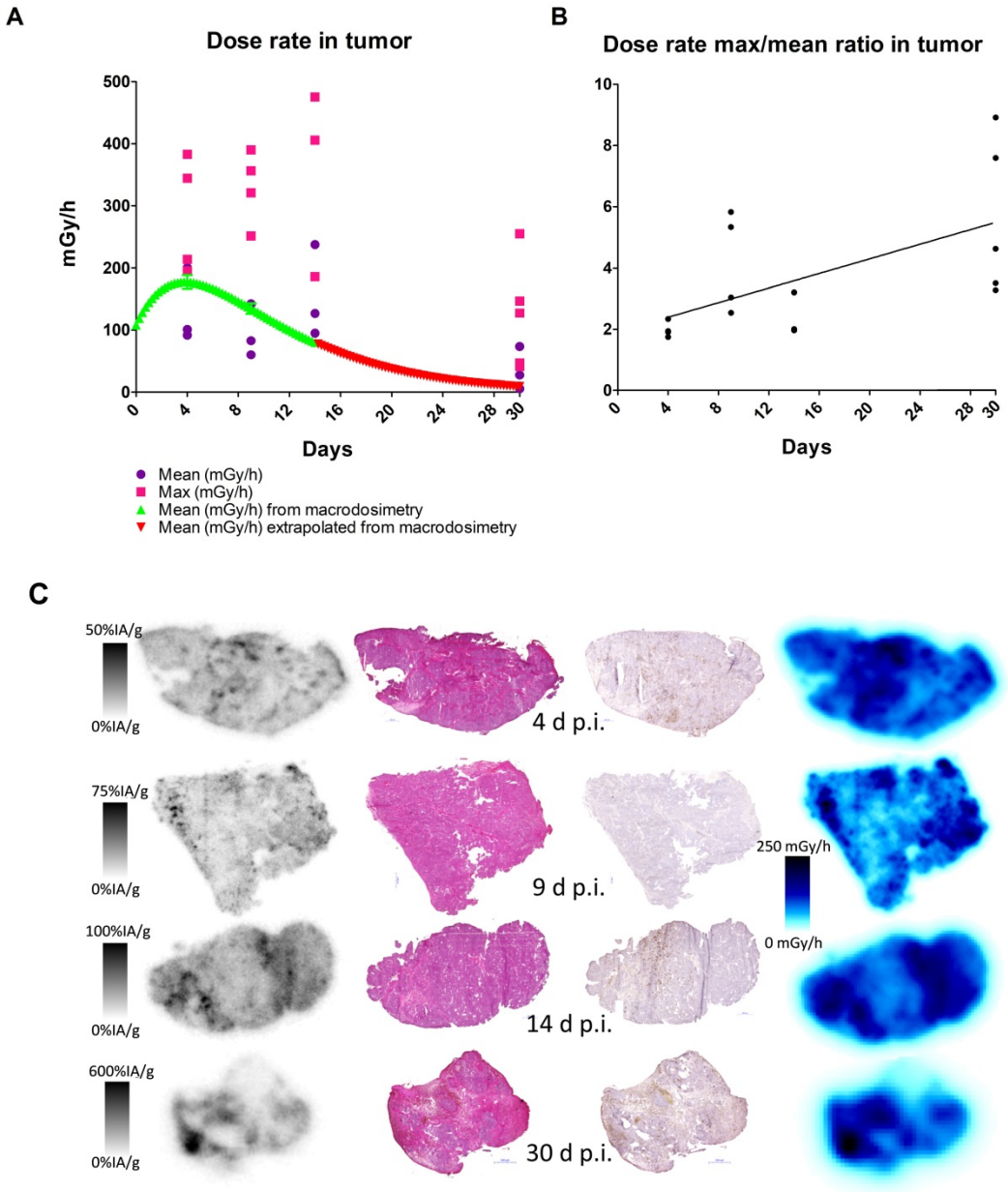

Figure 5. Absorbed dose and activity and absorbed dose rate distributions in tumor sections compared to histology and Ki-67 staining, 1 – 30 days after administration of ^{177}Lu-hu11B6. A. Mean and maximum absorbed dose rate as measured in tumor sections together with mean tumor absorbed dose from macrodosimetry calculated for the injected activity of the measured group. **B.** Absorbed dose rate ratio of Max to Mean. **C.** From left to right: Representative digital autoradiography images of activity uptake individually scaled to %IA/g. The same tissue sections stained with hematoxylin and eosin. Adjacent sections stained for the proliferation marker Ki-67. Finally, the distribution of absorbed dose rate at the moment of sacrifice, collectively scaled to mGy/h. From top to bottom 4, 9, 14 and 30 days after injection.

Histological scoring of tumor tissue showed similar homogenous staining of AR at all timepoints (Table 2). Staining for proliferation (Ki-67) and senescence (SA-β-gal activity) appears to be negatively correlated with low staining for Ki-67 at 9-14 days and high staining for SA-β-gal activity at 14 days (Table 2). Representative images of the SA-β-gal activity stainings can be found in the suppl. material. Although some variability was observed during the time course, an overall correlation was noted between increasing activity uptake and decreasing Ki-67 staining intensity (nadir at 9 and 14 days p.i.) suggesting that [^{177}Lu]hu11B6 inhibits cellular proliferation (Table 2 and Table 3). In addition, at later time-points higher activity was noted in fibrotic areas surrounded by regions of low Ki-67 staining. No activity uptake was found in necrotic tumor areas. (Figure 5C). Analysis of the mean AR staining intensity for each of the tissue section's cells ranged from 134 to 194 (arbitrary units). The results show that the AR expression level remained roughly constant over time up until two weeks but then at 30 days the remaining viable cells had significantly greater AR expression intensity ($p = 0.017$) compared to that of the pooled data from the 4-14 day time points and the controls (Figure 6A-B).

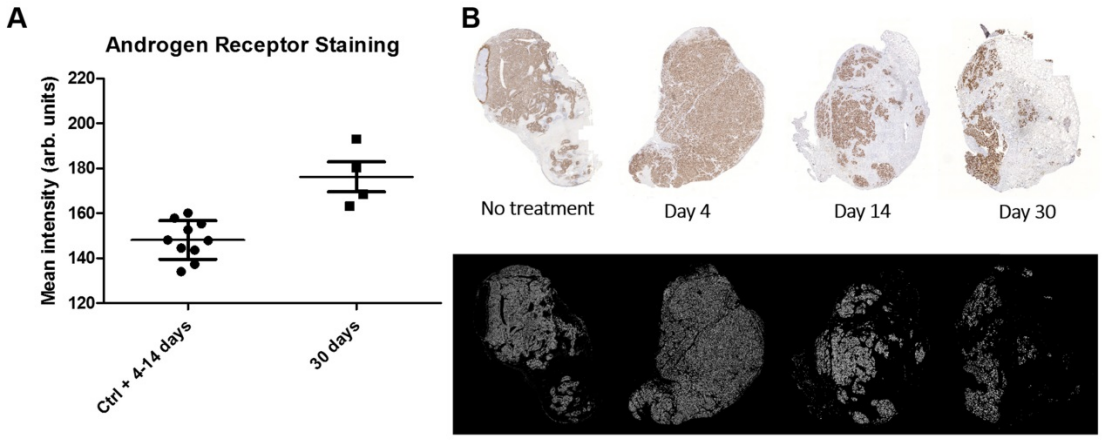

Figure 6. AR intensity analysis. A. Scatterplot with standard deviation and mean showing androgen receptor stain intensity which was pooled for controls (Ctrl) and 4-14 d and displayed separately for 30 d after initiation of radioimmunotherapy. Each point represents the intensity mean for a tumor section taken from a single animal. The AR intensity is significantly higher at 30 d indicating a AR flair phenomenon as result of DNA repair machinery. **B.** Representative tumor sections from which the data was derived. Top row shows the AR expression stain levels as a function of time. Bottom row shows the masks used to select AR expressing cells for AR expression analysis.

Table 2. Ki-67, AR immunohistochemistry and SA-β-gal activity staining. The intensity of the sections was graded independently by two different observers on a scale from nothing (-) to the highest intensity (+++). The average intensity is presented in the table.

Days p.i.	Average staining intensity		
	Ki-67	AR	SA-β-gal activity
4d	++	+++	++
9d	+	+++	++
14d	+	+++	+++
30d	++	+++	++
Control	+++	+++	+

Table 3. Correlation between nuclei stained for proliferation (Ki-67) and DAR image activity and absorbed dose rate

	Spearman correlation coefficient	
Time p.i. (d)	Ki-67 staining vs. activity	Ki-67 staining vs. absorbed-dose rate at the time of sacrifice
4	-0.548†	-0.523†
9	-0.750†	-0.672†
14	-0.409	-0.379
30	-0.343	-0.346

†$p < 0.01$

Discussion

Disabling the AR-signaling pathway has been the central pillar of PCa treatment since the seminal studies of Huggins and Hodges more than a half-century ago [31]. The major downfall with managing CRPC using this treatment strategy is the rapid development of resistance. Despite combining high affinity AR-blockers with steroid pathway synthesis inhibitors, the increased median survival in this patient group is only a couple of months. An alternative treatment path is to target potent cytotoxic agents to the sites of AR-driven PCa. We have addressed this unmet need for sustainable treatment effects by developing a radioimmunotherapeutic platform targeting hK2, a tightly AR-regulated prostate kallikrein. hK2 is a well characterized protease, with 80% amino acid homology to PSA. Other prostate-targeting agents lack specificity to prostate-derived tissue with significant off-target accumulation. Therefore, in vivo targeting of hK2 can be a significant improvement over PSMA, which has a high expression in non-target organs and in radiosensitive tissues such as the kidney. This issue is also prevalent among other targeting strategies, such as bombesin/gastrin-released peptide receptor (GRP-R) and prostate stem cell antigen (PSCA). Off-target accumulation limits the utility of cytotoxic radiolabeled small molecules and antibodies in treating prostate cancer and calls attention to the need for better engineered biologic delivery molecules. Furthermore, the clinical impact of AR-directed therapy on PSMA expression is poorly understood. PSMA expression has been shown to increase with AR inhibition [32] but also to decrease following long term ADT with an uneven metastatic expression (45% of metastatic lesions are PSMA-positive) [33]. Interestingly, in enzalutamide-resistant disease with glucocorticoid receptor cross-activated AR pathway, *KLK2* (hK2) expression, but not *KLK3* (PSA) or *FOLH1* (PSMA), is restored [34], suggesting hK2 as an optimal target for imaging and therapy.

Our previous reports, based on preclinical studies in advanced GEM models of prostate adenocarcinoma and metastatic disease, have shown that intravenously introduced radio- or fluorescently labeled 11B6 achieve uptake, internalization, and lysosomal degradation in hK2 expressing cells through an FcRn-mediated mechanism [13]. Cellular internalization provides permanent deposition of radionuclides in the cell. In this study we labeled hu11B6 with ^{177}Lu, generating [^{177}Lu]hu11B6, which

emits beta-particles at the site of the tumor. Compared to short-range alpha-emitters (such as Actinium-225, Bismuth-213 and Astatine-211), the long-ranging betas from [^{177}Lu]hu11B6 result in a crossfire effect. This could potentially be lethal to surrounding heterogeneous cell populations with lower AR and lower target expression. Thus even nearby cancer cells that do not internalize hu11B6 will be irradiated. The capability of hu11B6 to deliver payloads close to the nucleus, as compared to cell membrane binding targeting, is of high importance for the therapeutic efficacy when using alpha particle emitters. Following internalization of [^{177}Lu]hu11B6 to the nucleus, a contribution from short ranged conversion electrons to the resulting absorbed dose can also be expected. ^{177}Lu also emits two prominent easily imaged medium energy photons (113 and 208 keV at 6.8 and 10.4% abundance, respectively) which have been shown to produce images with a quantitative accuracy of better than 5-6% [35, 36] and can therefore be used in a theranostic approach to hK2 targeted RIT. Further, in a clinical setting, it is possible that some patients might not benefit from the use of this radioimmuoconjugate due to high serum levels of free hK2. However, this could then be determined with a simple blood test already conducted today.

Evaluating the therapeutic efficacy of [^{177}Lu]hu11B6 revealed that a single injection resulted in good therapeutic response with acceptable overall toxicity. The results are in line with our previously reported results based on a murine version of 11B6 [20]. Interestingly, the relationship between therapeutic efficacy, measured as log(RTS) and absorbed dose to the tumor, is similar for most administrated activities both in the present study and in adapted data from our previous report (Figure 4B). In clinical practice, potent and promising agents (such as Radium-223) are administered on a per-weight basis, without accounting for patient-specific disease characteristics or the absorbed dose needed at lesions to eradicate disease. Accounting for a dose-effect relationship in targeted radionuclide therapy is debated, although clinical studies have confirmed dose-effect relationships, they are not very strong and there are few preclinical studies that can demonstrate clear relationships [37, 38]. This could in part be due to the lack of accurate preclinical dosimetry models [37]. In our study, the administrated activity and absorbed dose versus log change in tumor volume (log(RTS)) generally demonstrated a clear and repeatable dose-effect relationship between tumor response and relapse (Figure 3A and Figure 4A-B). However, tumor specific uptake (%IA/g) acquired from SPECT data deviates from that seen at 14 d when using subtherapeutic amounts of activity (compare Figure 1C with 2B). This is because the volume of the xenograft decreases as an effect of therapy which means that the true absorbed dose to the remaining tumor probably is higher than the one calculated based on subtherapeutic activity biodistribution. A similar effect has been shown clinically in lymphoma patients [39]. However, at the same time the specific uptake in heart and liver is similar with therapeutic activities. The decrease in tumor volume and increase over time in specific uptake, as observed with SPECT imaging, confirms the functionality with respect to internalization, retention and therapeutic efficacy of [^{177}Lu]hu11B6. Our findings therefore further support a SPECT-based theranostic approach where pre-therapy treatment planning can predict normal organ toxicity and intratherapeutic dosimetry can predict the therapeutic efficacy. This highlights the need for robust and accurate dosimetry models in preclinical evaluation of RIT compounds for solid tumor treatment, thereby overcoming a significant deficiency in the existing practice of radiopharmaceutical therapy agent translation and application [40].

The heterogeneous absorbed dose distribution following RIT implies that some malignant cells, not directly targeted, could escape treatment. Or, conversely, that there are areas within the tumor with relatively high absorbed dose compared to the mean. In this study, some absorbed doses reach values of several hundred Gy, which could be an additional explanation for good therapeutic results. We therefore investigated the microdistribution of [^{177}Lu]hu11B6 and found a dose-effect relationship between the absorbed dose rate and the proliferation (Ki-67) in different areas of the xenograft as well as an, over time, increasing max-to-mean activity ratio between different parts of the tumor (Table 3, Figure 5B). However, though some tumor regions showed varying degrees of response, histological staining and absorbed dose rate distribution over time (Figure 5C) together with the drastic decrease in tumor volume reveals that large parts of the initially targeted tumor are efficiently treated. The SPECT data on tumor specific uptake and the data on changing max-to-mean activity ratio support one another and confirms the retention of the radionuclide in the tumor over time. The retention of the radionuclide and decreasing tumor volume is likely the reason for retained absorbed dose rates within the tumor up to 14 days after injection (Figure 5C). Therapeutic effect in an area of the tumor could thus lead to higher absorbed doses in other parts of the tumor due to the crossfire effect. The results show that both macro- and small-scale dosimetry approaches and methods are useful to fully understand the therapeutic response.

Uptake of [^{177}Lu]hu11B6 over time could be further stimulated by an increase in the AR axis activity as an effect of therapy. The change in mean AR staining intensity at 30 days points to a selection mechanism or some pathway upregulation that results in a net per-cell increase of AR protein level following irradiation. As suggested in previous studies, this could be due to a general increase in DNA repair mechanisms dependent on AR upregulation as a response to irradiation. This phenomenon would then manifest itself later with low LET beta-particles, post 14 days as opposed to earlier reported 6-14 days for high LET alpha particles [14]. Or it could be explained by the clonal selection of cell lineages that use AR upregulation as a mechanism of resistance. In our case this cell population would then become dominant enough at 30 days to be detected as an increase in mean AR staining intensity. This theory could further explain the difference seen between low LET beta-particles in this study and previously studied high LET alpha particles. Irradiation with low LET beta-particles results predominantly in so called sub-lethal damage e.g. SSB, as compared to high LET alpha particles which mainly give rise to DSB. High LET irradiation has also been shown to induce more apoptosis compared to low LET irradiation [41] and to a faster cell death progression due to more severe damage. Two weeks into therapy we see large areas of cells stained for SA-β-gal activity (Table 2) and low proliferation, which together indicates senescence [42, 43]. A senescent cellular state is an indefinite cell cycle arrest as a consequence of irreparable sub-lethal damage e.g. DNA damage or oxidative stress and the inability to enter apoptosis [42]. Large numbers of senescent cells in LNCaP xenografts after therapy with low LET beta-particles could mask a clonal selection of lineages with high AR expression by influencing the result of measured mean AR status so that this phenomenon appears to be delayed when compared to therapy with high LET alpha-particles. The AR flair phenomenon could therefore be the result of cells in general responding to DNA damage by upregulation of DNA repair pathways that involve the AR or from subpopulations of cells that do so.

A potential therapeutic strategy, encouraged by the enhanced AR expression several weeks after onset of therapy, is to perform serial administration of radiolabeled hu11B6. Our findings that AR protein levels are increasing after [^{177}Lu]hu11B6 therapy (Figure 6), support earlier findings of increasing levels of AR mRNA following [^{225}Ac]hu11B6 therapy [14] and points at a persistent and high AR signaling in remaining cells following irradiation and hk2 targeted RIT. This means that the response to treatment, instead of just conveying resistance, could lead to continuously high uptake of hu11B6. However, it remains to be further investigated how high and low LET particle emissions, as well as different absorbed dose rates, differ in their influence on this radiobiological phenomenon. However, besides serial administration, the parallel use of different radionuclides with different LET is therefore also of interest for further development. The combination of therapy with both beta emitters and alpha emitters, the later with high linear energy transfer and high relative biological effect, as well as external beam radiation therapy could be an interesting expansion of the hK2 targeting RIT hu11B6 platform.

Conclusion

This preclinical study with ^{177}Lu-radiolabeled immuno-targeting of hK2 demonstrated good therapeutic efficacy with one of the treated groups showing a large reduction in tumor volume together with reversible myelotoxicity. The tumor response was dependent on administered activity and delivered absorbed dose, as evaluated on both macro and small-scale dosimetric levels. These results, together with the findings of persistent hK2 and increasing AR levels support the use of SPECT imaging approaches for dosimetry and therapy evaluation. Interestingly, hu11B6 radiolabeled with 177-lutetium, a low LET beta-emitter, appeared to induce a similar AR flair phenomenon, albeit at a later time point, in remaining prostate cancer cells as was previously seen after [^{225}Ac]hu11B6 treatment and irradiation with a ^{137}Cs source. In view of previously published data, this study suggests that this could be due to either a general DNA repair mechanism or because of clonal lineage selection. The phenomenon could potentially be used in therapeutic strategies with serial [^{177}Lu]hu11B6 or parallel/co-administration of [^{177}Lu]hu11B6 and [^{225}Ac]hu11B6.

Abbreviations

[^{225}Ac]hu11B6: ^{225}Ac-DOTA-hu11B6
[^{177}Lu]hu11B6: ^{177}Lu-DTPA-hu11B6
[^{177}Lu]IgG$_1$: ^{177}Lu-DTPA-IgG$_1$
^{225}Ac: Actinium-225
AR: Androgen receptor
GRP-R: Bombesin/gastrin-released peptide receptor
CRPC: Castration resistant prostate cancer
CT: Computed tomography
DTPA: Diethylenetriaminepentaacetic acid
DAR: Digital autoradiography
DPK: Dose point kernel
fc: Fragment crystallizable

hK2: Human kallikrein related peptidase 2
LET: Linear energy transfer
log(RTS): Logarithmic Relative Tumor Size value
^{177}Lu: Lutetium-177
FcRn: Neonatal Fc receptor
%IA/g: Percent injected activity per gram/ specific uptake
PET: Positron emission tomography
PSA: Prostate specific antigen
PSCA: Prostate stem cell antigen
RIT: Radioimmunotherapy
RBC: Red blood cell count
RTS: Relative Tumor Size
PLT: Platelets
SPECT: Single-photon emission computed tomography
SA: Specific activity
WBC: White blood cell count

Acknowledgments

This study was performed with generous support from the Swedish Cancer Foundation, the Swedish Science Council, Mrs. Berta Kamprad's Foundation, Gunnar Nilsson's Foundation, Percy Falk's Foundation. The authors would like to thank Emma Mellhammar and Anna Stenvall for help with SPECT/CT acquisition and Wahed Zedan for help with the sectioning of paraffin embedded tissue. Lund University Bioimaging Center (LBIC), Lund University is gratefully acknowledged for providing experimental resources.

Supplementary Material

Supplementary figures and tables.
http://www.thno.org/v09p2129s1.pdf

Competing interests

Sven-Erik Strand, David Ulmert and Dan Thorek are shareholders in Diaprost AB who owns the commercial rights for hu11B6 and hold patents for its applications. Sven-Erik Strand and David Ulmert are authors on several patents protecting the use of radiolabeled 11B6. Oskar Vilhelmsson Timmermand and Thuy Tran are the co-authors of a patent, held by Diaprost AB, on humanized 11B6.

References

1. Visakorpi T, Hyytinen E, Koivisto P et al. In vivo amplification of the androgen receptor gene and progression of human prostate cancer. Nat Genet. 1995; 9(4): 401-6.
2. Jurcic JG, Larson SM, Sgouros G et al. Targeted alpha particle immunotherapy for myeloid leukemia. Blood. 2002; 100(4): 1233-9.
3. Witzig TE, Gordon LI, Cabanillas F et al. Randomized controlled trial of yttrium-90-labeled ibritumomab tiuxetan radioimmunotherapy versus rituximab immunotherapy for patients with relapsed or refractory low-grade, follicular, or transformed B-cell non-Hodgkin's lymphoma. J Clin Oncol. 2002; 20(10): 2453-63.
4. Gaertner FC, Halabi K, Ahmadzadehfar H et al. Uptake of PSMA-ligands in normal tissues is dependent on tumor load in patients with prostate cancer. Oncotarget. 2017; 8(33): 55094-55103.
5. Rahbar K, Ahmadzadehfar H, Kratochwil C et al. German Multicenter Study Investigating ^{177}Lu-PSMA-617 Radioligand Therapy in Advanced Prostate Cancer Patients. J Nucl Med. 2017; 58(1): 85-90.
6. Kratochwil C, Giesel FL, Stefanova M et al. PSMA-Targeted Radionuclide Therapy of Metastatic Castation-Rersistant Prostate Cancer with ^{177}Lu-Labeled PSMA-617. J Nucl Med. 2016; 57(8): 1170-6.
7. Tagawa ST, Milowsky MI, Morris M et al. Phase II study of Lutetium-177-labeled anti-prostate-specific membrane antigen monoclonal antibody J591 for metastatic castration-resistant prostate cancer. Clin Cancer Res. 2013; 19(18): 5182-91.
8. Young CY, Andrews PE, Montgomery BT et al. Tissue-specific and hormonal regulation of human prostate-specific glandular kallikrein. Biochem. 1992; 31(3): 818-24.
9. Lawrence MG, Lai J, Clements JA. Kallikreins on steroids: structure, function, and hormonal regulation of prostate-specific antigen and the extended kallikrein locus. Endocr Rev. 2010; 31(4): 407-46.
10. Kollara A, Diamandis EP, Brown TJ. Secretion of endogenous kallikreins 2 and 3 by androgen receptor-transfected PC-3 prostate cancer cells. J of Steroid Biochem Mol Biol. 2003; 84(5): 493-502.
11. Uhlen M, Oksvold P, Fagerberg L et al. Towards a knowledge-based Human Protein Atlas. Nat Biotechnol. 2010;28(12):1248-50.
12. Grauer LS, Finlay JA, Mikolajczyk SD et al. Detection of human glandular kallikrein, hK2, as its precursor form and in complex with protease inhibitors in prostate carcinoma serum. J Androl. 1998; 19(4): 407-11.
13. Thorek DL, Watson PA, Lee SG et al. Internalization of secreted antigen-targeted antibodies by the neonatal Fc receptor for precision imaging of the androgen receptor axis. Sci Transl Med. 2016; 8(367): 367ra167.
14. McDevitt MR, Thorek DLJ, Hashimoto T et al. Feed-forward alpha particle radiotherapy ablates androgen receptor-addicted prostate cancer. Nat Commun. 24; 9(1): 1629.
15. Polkinghorn WR, Parker JS, Lee MX et al. Androgen receptor signaling regulates DNA repair in prostate cancers. Cancer Discov. 2013; 3(11): 1245-53.
16. Goodwin JF, Schiewer MJ, Dean JL et al. A hormone-DNA repair circuit governs the response to genotoxic insult. Cancer Discov. 2013; 3(11): 1254-71.
17. Aghevlian S, Boyle AJ, Reilly RM. Radioimmunotherapy of cancer with high linear energy transfer (LET) radiation delivered by radionuclides emitting α-particles or auger electrons. Adv Drug Deliv Rev. 2017; 109: 102-118.
18. Soyland C, Hassfjell SP. Survival of human lung epithelial cells following in vitro alpha-particle irradiation with absolute determination of the number of alpha-particle traversals of individual cells. Int. J. Radiat. Biol. 2000; 76(10): 1315-22.
19. Evaluation of the serum stability and in vivo biodistribution of CHX-DTPA and other ligands for yttrium labeling of monoclonal antibodies. Camera L, Kinuya S, Garmestani K et al. J Nucl Med. 1994; 35(5): 882-9.
20. Vilhelmsson Timmermand O, Larsson E, Ulmert D et al. Radioimmunotherapy of prostate cancer targeting human kallikrein-related peptidase 2. EJNMMI Res. 2016 ;6(1): 27.
21. Areberg J, Wennerberg J, Johnsson A et al. Antitumor effect of radioactive cisplatin (^{191}Pt) on nude mice. Int J Radiat Oncol Biol Phys. 2001; 49(3): 827-32.
22. Rueden CT, Schindelin J, Hiner MC et al. ImageJ2: ImageJ for the next generation of scientific image data. BMC Bioinformatics. 2017; 18(1): 529.
23. Larsson E, Ljungberg M, Martensson L et al. Use of Monte Carlo simulations with a realistic rat phantom for examining the correlation between hematopoietic system response and red marrow absorbed dose in Brown Norway rats undergoing radionuclide therapy with (^{177})Lu- and (90)Y-BR96 mAbs. Med Phys 2012; 39(7): 4434-43.
24. Larsson E, Strand SE, Ljungberg M et al. Mouse S-factors based on Monte Carlo simulations in the anatomical realistic Moby phantom for internal dosimetry. Can. Biother Radiopharm 2007; 22(3): 438-42.
25. Sgouros G. Bone marrow dosimetry for radioimmunotherapy: theoretical considerations. J Nucl Med 1993; 34(4): 689-94.
26. Örbom A, Ahlstedt J, Serén T et al. Characterization of a double-sided silicon strip detector autoradiography system. Med Phys. 2015; 42(2): 575-84.
27. Örbom A, Eriksson SE, Elgström E et al. The intratumoral distribution of radiolabeled ^{177}Lu-BR96 monoclonal antibodies changes in relation to tumor histology over time in a syngeneic rat colon carcinoma model. J Nucl Med. 2013; 54(8): 1404-10.
28. Schneider CA, Rasband W, Eliceiri KW. NIH Image to ImageJ: 25 years of image analysis. Nat Met. 2012; 9: 671-675.
29. Tuominen VJ, Ruotoistenmäki S, Viitanen A et al. ImmunoRatio: a publicly available web application for quantitative image analysis of estrogen receptor (ER), progesterone receptor (PR), and Ki-67. Breast Cancer Res. 2010; 12(4): R56.
30. Martensson L, Wang Z, Nilsson R et al. Determining maximal tolerable dose of the monoclonal antibody BR96 labeled with ^{90}Y or ^{177}Lu in rats: establishment of a syngeneic tumor model to evaluate means to improve radioimmunotherapy. Clin Can Res. 2005; 11(19 Pt 2): 7104-08.
31. Ferraldeschi R, Welti J, Luo J, Attard G, de Bono JS. Targeting the androgen receptor pathway in castration-resistant prostate cancer: progresses and prospects. Oncogene. 2015; 34(14): 1745–1757.
32. Evans MJ, Smith-Jones PM, Wongvipat J et al. Noninvasive measurement of androgen receptor signaling with a positron-emitting radiopharmaceutical

that targets prostate-specific membrane antigen. Proc Natl Acad Sci U S A. 2011; 108(23): 9578-82.
33. Afshar-Oromieh A, Debus N, Uhrig M et al. Impact of long-term androgen deprivation therapy on PSMA ligand PET/CT in patients with castration-sensitive prostate cancer. Eur J Nucl Med Mol Imaging. 2018; 45(12): 2045-2054.
34. Arora VK, Schenkein E, Murali et al. Glucocorticoid receptor confers resistance to antiandrogens by bypassing androgen receptor blockade. Cell. 2013; 155(6): 1309-22.
35. Uribe CF, Esquinas PL, Tanguay J et al. Accuracy of ^{177}Lu activity quantification in SPECT imaging: a phantom study. EJNMMI Phys. 2017; 4: 2.
36. Gustafsson J, Brolin G, Cox M et al. Uncertainty propagation for SPECT/CT-based renal dosimetry in ^{177}Lu peptide receptor radionuclide therapy. Phys Med Biol. 2015; 60(21): 8329-46.
37. Pouget JP, Lozza C, Deshayes E et al. Introduction to radiobiology of targeted radionuclide therapy. Front Med (Lausanne) 2015; 2: 12.
38. Strigari L, Konijnenberg M, Chiesa C et al. The evidence base for the use of internal dosimetry in the clinical practice of molecular radiotherapy. Eur J Nucl Med Mol Imaging. 2014; 41(10): 1976-88.
39. Hindorf C, Lindén O, Stenberg L et al. Change in tumor-absorbed dose due to decrease in mass during fractionated radioimmunotherapy in lymphoma patients. Clin Cancer Res. 2003; 9(10 Pt 2): 4003-6.
40. Ljungberg M, Celler A, Konijnenberg MW et al. MIRD Pamphlet No. 26: Joint EANM/MIRD Guidelines for Quantitative ^{177}Lu SPECT Applied for Dosimetry of Radiopharmaceutical Therapy. J Nucl Med. 2016; 57(1): 151-62.
41. Niemantsverdriet M, van Goethem MJ, Bron R et al. High and Low LET Radiation Differentially Induce Normal Tissue Damage Signals. Int J Rad Onc 2012;83(4):1291-7
42. Ewald JA, Desotelle JA, Wilding G et al. Therapy induced senescence in Cancer. J Natl Cancer Instm. 2010; 102: 1536-1546.
43. Dimri GP, Lee X, Basile G et al. A Biomarker that identifies senescent human cells in culture and in aging skin invivo. Proc Natl Acad Sci USA. 1995; 92(20): 9363-9367.